nature communications

Article

https://doi.org/10.1038/s41467-025-60298-z

Entropy-driven difference in interfacial water reactivity between slab and nanodroplet

Received: 6 October 2024

Accepted: 19 May 2025

Published online: 05 June 2025

Check for updates

Shiwei Chen[1], Jiabao Zhu[1], Jifan Li[1], Pan Guo[2] ✉, Jinrong Yang[1] ✉ & Xiao He[1,3,4] ✉

Interfacial water activity plays a critical role in governing chemical reactivity and catalytic efficiency, yet a quantitative understanding of how hydrogen-bond (H-bond) network structure influences this reactivity remains limited. Herein, we employ ab initio molecular metadynamics simulations to delineate the relationship between the H-bond network and the reactivity of interfacial water molecules at the slab and nanodroplet systems. Interfacial water at nanodroplets, characterized by microscopic inhomogeneity, tends to adopt a donor–acceptor dimer configuration, in contrast to the more homogeneous H-bond network at the slab. This disparity in local structure, corroborated by the quantified differences in solvation configurational entropy, results in a reduction of the reaction free energy barrier by 1–2 kcal·mol^{-1} at the slab interface, corresponding to an order-of-magnitude enhancement in reaction rate. These results provide a fresh perspective to understand the interfacial water reactivity and highlight the critical role of H-bond network in optimizing catalytic performance.

The hydrogen-bond (H-bond) networks and orientation of water molecules at interfacial environments have become a compelling topic in the field of catalysis[1–4]. These networks with ordered O-H dangling bonds pointing toward the vapor phase structures generate a strong electric field capable of accelerating the reaction rate by orders of magnitude ranging from one to six without the need for any chemical reagent, compared to their reaction rates in bulk water solution[5–8]. For example, Xie's group demonstrated that the decrease barrier of aza-Michael addition reaction between methylamine and acrylamide on air-water surface of condensing microdroplet can be attributed to such interfacial electric field[7], which has been estimated to be about 0.1 V/Å based on the vibrational Stark effect of a nitrile-bearing fluorescent probe[8]. Furthermore, recent studies reveal that the peculiar topologies of H-bond network may promote interfacial charge transfer, providing valuable insights for engineering more efficient catalytic materials. For instance, Li et al. uncovered that the reduced hydrogen evolution reaction kinetics on Pt in alkaline media is driven by the altered connectivity of H-bond network within the electric double layer, offering key insights into how electric double layer structure can affect catalytic performance[9]. Therefore, a deeper understanding of the mechanisms by which H-bond network facilitate reaction will potentially enable to fine-turn the interfacial microenvironment, which in turn leads to the cost-effective production of innovative materials and the advancement of green chemical synthesis processes.

Various experimental techniques, such as Fourier Transform Infrared (FTIR) spectroscopy[10–13], scanning tunneling microscopy[14–16], in situ Raman spectroscopy[17–19], X-ray absorption spectroscopy[20–24], and sum-frequency generation (SFG) spectroscopy[25–29] have been used to investigate the structural and vibrational characteristics of water structure at interfacial environments. For example, Wang et al.

[1]Shanghai Engineering Research Center of Molecular Therapeutics and New Drug Development, Shanghai Frontiers Science Center of Molecule Intelligent Syntheses, School of Chemistry and Molecular Engineering, East China Normal University, 3663 North Zhongshan Rd, Shanghai 200062, China. [2]Department of Physics, Shanghai Key Laboratory of High Temperature Superconductors, International Centre of Quantum and Molecular Structures, Shanghai University, Shanghai 200444, China. [3]Chongqing Key Laboratory of Precision Optics, Chongqing Institute of East China Normal University, Chongqing 401120, China. [4]New York University-East China Normal University Center for Computational Chemistry, New York University Shanghai, Shanghai 200062, China.
✉e-mail: guopan@shu.edu.cn; jryang@chem.ecnu.edu.cn; xiaohe@phy.ecnu.edu.cn

employed in situ Raman spectroscopy to elucidate the relationship between interfacial water structure and the rate of the hydrogen evolution reaction[17]. Their findings revealed a significant increase in reaction kinetics, as evidenced by a reduction in the Tafel slope from 496 to 156 mV·dec^{-1}. This change is attributed to the transition of interfacial water structure from a disordered arrangement to a more ordered structure, corroborated by the enhanced intensity of the band observed at approximately 550 cm^{-1}. FTIR spectroscopy has also been employed to study the influence of H-bond networks on photoactivity in water-splitting. Verduci et al. reported a remarkable 5-fold increase in photoactivity, which they attributed to alterations in the H-bond network at the B-doped TiO_2 surface[10]. This surface displayed H-bond motifs that were 20% to 90% richer in donor-acceptor (DA) populations than in double donor-acceptor (DDAA) configurations, leading to the formation of nearly linear H-bonded chains. Despite these insights, a quantitative relationship between H-bond structure and reaction activity remains challenging to define due to the interference from bulk water and the inherent complexity of interfacial environments.

Water molecules at the air-water interface exhibit a heightened heterogeneity and dynamic behavior compared to their bulk counterparts, which significantly amplifies their chemical activity[30,31]. This unique interfacial behavior has been the subject of various experimental techniques aimed at unraveling the structural and dynamic properties of these molecules. Hsieh et al.[32] utilized sum-frequency generation (SFG) spectroscopy to delineate the vibrational frequencies at the air-water interface, identifying a broad negative peak above 3200 cm^{-1} and a minor positive peak below 3200 cm^{-1}. Their results indicated a substantial reduction in intermolecular coupling among water molecules at the interface, in contrast to the homogeneous coupling observed in bulk water. This suggests that the water molecules at the interface are more loosely associated, which makes them more susceptible to a variety of accelerated chemical reactions, particularly pertinent to atmospheric chemistry and on-water catalysis. Thus, comprehending the mechanisms underlying the acceleration of reactions at air-water interface is essential.

In both theoretical and experimental contexts, nanodroplets and slab represent the primary systems utilized to investigate air-water interface reactions[33,34]. Characteristics shared by both slab and microdroplets include high surface-area-to-volume ratios and a high degree of reagent confinement. Using paper spray and nano electrospray ionization combined with mass spectrometry, Cook's group revealed the significant role of interfacial processes in 15-fold acceleration of C-C bond-formation reaction at the slab and nanodroplets[35]. Employing ab initio calculations with high precision, an electrostatic potential of 3 to 4.5 V was measured on the air-water interface of slab and droplets, which could be the driving force behind the observed acceleration[3,36]. Additionally, both nanodroplets and slab have the similar fast solvent evaporation, which could accelerate the reaction[33]. However, significant differences exist in the H-bond networks of various sizes of nanodroplets and slab. For example, Mizuse et al., through infrared spectroscopy of $H^+(H_2O)_n$ and density functional calculations, noted that the relative intensity of the free OH band decreases with increasing nanodroplet size, suggesting an increasing coordination number of water molecules[37]. While significant strides have been made in understanding the behavior of water at this interface, the complexity of these interactions and their influence on reaction dynamics in quantitative terms remain an area ripe for further exploration.

In this work, we performed ab initio molecular metadynamic simulation to characterize the interplay between the H-bond networks and reactivity of interfacial water on slab and nanodroplet. Our findings reveal that the interfacial water molecules in nanodroplets, characterized by microscopic inhomogeneity, tend to become trapped in donor-acceptor dimers. This entrapment significantly impairs their ability to participate in interfacial reactions, in contrast to the more homogeneous H-bond network type observed in slab. The free energy barrier for interfacial water to participate in reactions on slab system is reduced by approximately 1–2 kcal/mol compared to the nanodroplet with a 10 Å radius, resulting in a reaction rate that is an order of magnitude faster on slab system. This pronounced difference in reactivity can be attributed to the quantified variation in solvation configurational entropy between nanodroplets and slab surfaces at ambient temperature. Furthermore, through machine learning potential (MLP)[38], interfacial water structures are analyzed based on 10 ns ab initio machine-learning-assisted simulations of nanodroplet systems, including $(H_2O)_{19}$, $(H_2O)_{21}$, $(H_2O)_{30}$, $(H_2O)_{50}$, $(H_2O)_{100}$, $(H_2O)_{200}$, $(H_2O)_{300}$, and $(H_2O)_{500}$, as well as bulk and slab systems. The vibrational density of states (VDOS) reveals a linear relationship between the free O-H stretching frequency and the inverse-square of the nanodroplet size, and the variation in interfacial coordination unsaturation as a function of nanodroplet size fall within the prediction of Gibbs-Thomson equation. The restructuring of the H-bond networks with decreased sizes makes the distinct rotational dynamics of interfacial water molecules becoming faster, accompanying with the faster translation of interfacial water through fluctuation-dissipation mechanism. These results offer new insights into the reactivity of interfacial water, underscoring the pivotal role of the H-bond networks in enhancing catalytic efficiency.

Results

Interfacial water reactivity

Theoretically, both nanodroplets and slab system, as the archetypal model of microdroplet, have been instrumental in deciphering the acceleration mechanism of various chemical reactions. However, the subtle distinctions in their catalytic effects have not been rigorously examined. We fill this gap by proposing a novel physicochemical picture to elucidate the anomalous reduction in reaction barrier on slab compared to nanodroplet, as illustrated in Fig. 1a, which is intricately linked to a general phenomenon involving the alteration in the H-bond network as the potential descriptor for the interfacial water reactivity. Specifically, the rearrangement configuration and distribution of H-bonds are pivotal in reshaping the energy landscape. We denote the H-bond donor as D and the acceptor as A. For example, the DA configuration, featuring a single H-bond donor and a single H-bond acceptor, give rise to one free O-H bond and one O-H bond engaged in H-bond (H-bonded O-H bond). From a static structure perspective, the length of O-H bond involved in H-bond usually adheres to the concept of asymmetrical H-bond cooperativity and polarizability, causing a reduction in the average length of free O-H bonds compared with H-bonded O-H bonds[39]. At the air-water interface, H-bonded O-H bonds exhibit an average length of 0.988 Å, which is 0.013 Å longer than free O-H bonds (0.975 Å). This structural difference induces an energy disparity of 0.74 kcal/mol between H-bonded and non-H-bonded water molecules at the single-point level of CCSD(T)/aug-cc-pV5Z.

Based on the above results, Fig. 1b illustrates a new perspective that the reduction in nanodroplet size leads to an increase in entropy by liberating water molecules from hydrogen bonding constraints, thus promoting a heterogeneous H-bond network topology and a decrease of surface tension. The surface tension of slab system is reported to be around 72 mN/m at 300 K[40], and Li et al.[41] employed molecular dynamics simulations to demonstrate that the surface tension of the droplets decreases from 66 to 19 mN/m as the radius of nanodroplets changes from 24 to 6 nm. As a result, the dominant DA configuration in nanodroplets suggests a higher density of free OH bonds at the air-water interface. Conversely, the slab system displays an almost equal distribution of the DA, DDA (double H-bond donors and a single acceptor), DAA (single donor and double acceptors), and DDAA (double donors and double acceptors) configurations, indicating a more H-bonded O-H bond. Increased hydrogen bonding weakens the covalent OH bond in water, which might help lower the free energy

barrier for reactions in the slab geometry. Notably, the single point energy of a water molecule with free OH bond is 0.74 kcal/mol lower than that of a water molecule with H-bonded OH bonds, and nanodroplet $(H_2O)_{100}$ have a greater number of the free O-H bond of interfacial water relative to the slab system. This energy disparity requires additional free energy to overcome the stabilization of the free OH bonds, which in turn affects the interfacial reactivity. Our findings indicate that the free energy required for reactions at the air-water interface of nanodroplets is higher compared to slab system, due to the need to break the original O-H bond length associated with the solvation entropy. As such, the entropy plays a significant role in the observed discrepancies in reaction free energy between nanodroplets and slab system.

The comparison in the free energy profiles of three interfacial water participation reactions shows a marked preference for reactions to proceed on slab system rather than nanodroplets. Utilizing the coordination number of all hydrogen atoms surrounding the oxygen atom as the collective variable (CV), we observe that the free energy barrier for water self-dissociation is lower in the slab system containing 128 water molecules by ~1.9 kcal/mol, compared to a nanodroplet of $(H_2O)_{100}$, as shown in Fig. 1c. According to the Arrhenius equation, the difference in the free energy barrier of 1.9 kcal/mol for water self-dissociation between slab and nanodroplet leads to a reaction rate difference of approximately 25-fold at room temperature. This trend is further substantiated by the free energy profile of SO_2 hydrolysis (Fig. 1d), which increases by approximately 1.8 kcal/mol when transitioning from the slab system to the nanodroplet $(H_2O)_{100}$. Similarly, the free energy profile associated with hydration reaction increases by approximately 1.4 kcal/mol when moving from the slab system to the nanodroplet $(H_2O)_{100}$, as depicted in Fig. 1e. Additionally, the free energies of these reactions at the air-water interface are significantly lower than that in the gas phase (Supplementary Fig. 7).

To elucidate the intricate dynamics of H-bond networks during the water self-dissociation reaction, a comparative case study was conducted between a slab system and a nanodroplet model. The slab system exhibits the self-dissociation process initiated at 10 ps and completed at 19 ps (Fig. 2a). O1 and O2 represent the oxygen atoms that have lost and gained protons, respectively, while H1 denotes the transferred proton. During the proton transfer event, the water molecule acting as the proton donor adopts a DAA configuration, and an adjacent water molecule accepting this proton assumes a DDA configuration. As observed in Fig. 2b, the coordination number begins to fluctuate around 10 ps and decreases to approximately 1.3 at 19 ps. The distance of O1-H1 keeps at 1 Å and suddenly increases to 1.4 Å at about 10 ps, while the distance of O2-H1 decreases from 2 to 1.4 Å, indicating the initiation of proton transfer. Ultimately, at approximately 19 ps, the O2-H1 distance decreases to 1 Å, whereas the O1-H1 distance increases to 2 Å, indicating a significant rearrangement of proton. The water self-dissociation within the nanodroplet commences at 15 ps and concludes by approximately 22 ps (Fig. 2e). Throughout the proton transfer process, both the proton donor and acceptor of water molecules undergo the transformation from DA to DDA configuration. Figure 2f shows that the coordination number starts to fluctuating around 15 ps and drops to about 1.3 at 22 ps. The distance of O1-H1 increases from 1 Å to 1.5 Å at 22 ps, while the distance of O2-H1 decreases to 1 Å, signifying the completion of the water self-dissociation process. As shown in Fig. 2c, d the H-bond types of the dissociating water molecules on the slab remain relatively stable

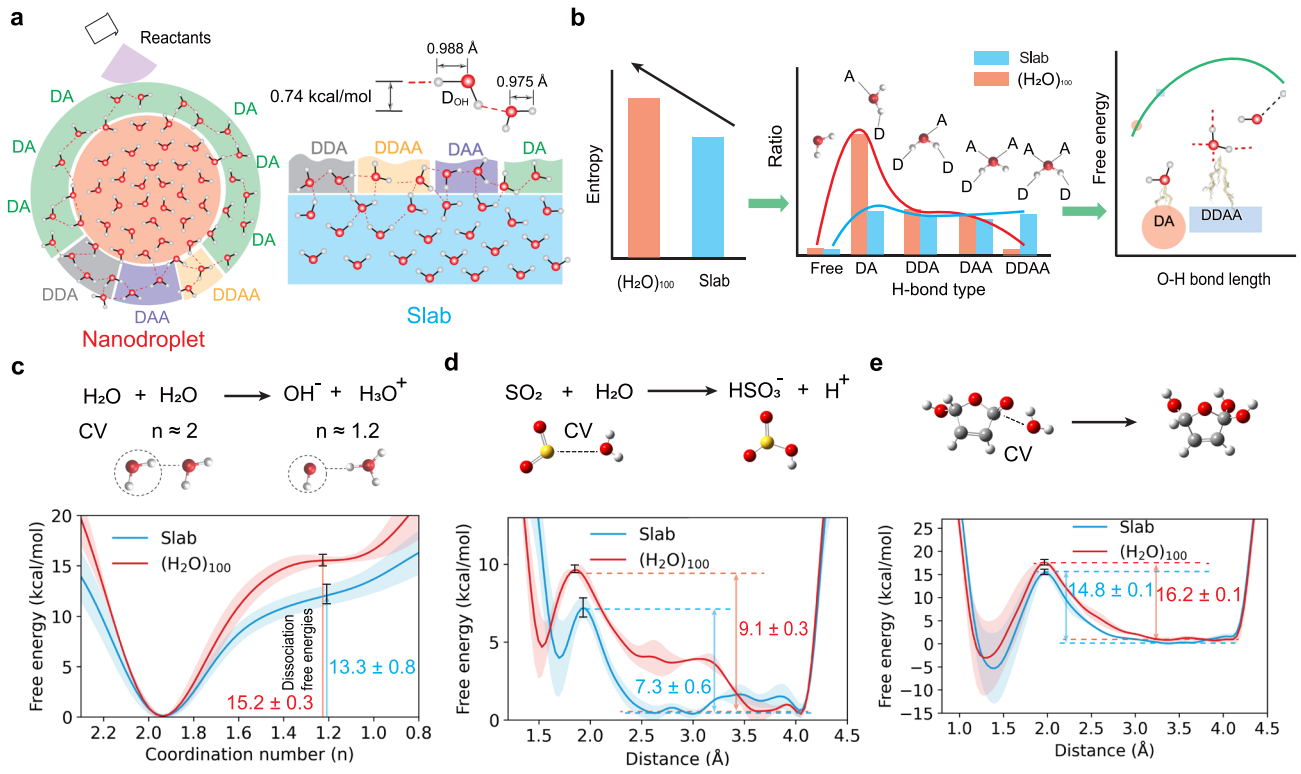

Fig. 1 | Discrepancy between the reaction energy profiles at the slab system and nanodroplet $(H_2O)_{100}$. **a** Schematic illustration of reactants at the air-water interface of nanodroplet $(H_2O)_{100}$ and slab system, where H-bond network of water molecules near the surface are represented. This physicochemical picture was created using Adobe Illustrator. **b** The quantitative interplay between entropy and H-bond type determines the reaction free energy profile at the air-water interface. Free energy profiles for (**c**) water self-dissociation, **d** the hydrolysis of SO_2 and (**e**) hydration reaction of furanone at air-water interface of the slab system (blue) and $(H_2O)_{100}$ (red), respectively. The collective variables (CV) for (**c**) water self-dissociation, **d** the hydrolysis of SO_2 and **e** hydration reaction of furanone are the coordination number, the distance between S and O, and the distance between C and O, respectively. The shaded areas represent the standard deviation from three independent simulations.

https://doi.org/10.1038/s41467-025-60298-z

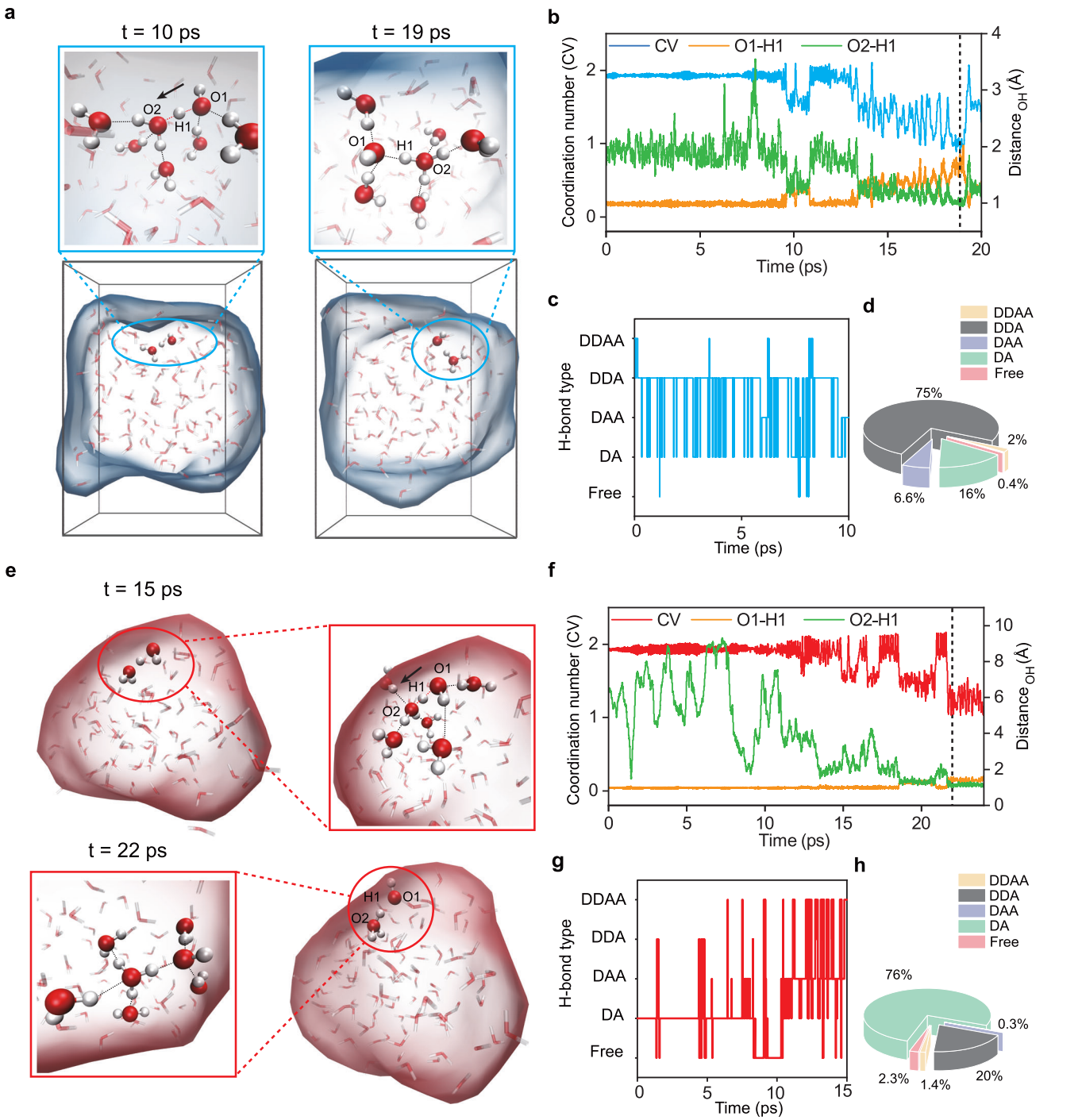

Fig. 2 | Reaction process of water self-dissociation at the slab system and nanodroplet $(H_2O)_{100}$. Snapshot structures taken from the metadynamics-biased ab initio molecular dynamics (AIMD) simulations of the water self-dissociation on (**a**) the slab system and (**e**) nanodroplet $(H_2O)_{100}$. The time evolution of coordination number and distance of O-H for (**b**) the slab system and (**f**) nanodroplet $(H_2O)_{100}$. The time evolution of H-bond type involved in the reaction process for (**c**) the slab system and (**g**) nanodroplet $(H_2O)_{100}$. The ratio of the H-bond type for the react water molecule on (**d**) the slab system and (**h**) nanodroplet $(H_2O)_{100}$ without further adjustment or correction for bias.

throughout the process. However, as shown in Fig. 2g, the dissociating water molecules on the nanodroplet initially exhibit a predominance of DA type H-bonds, which undergoes significant changes just prior to the onset of dissociation. This shift from DA to DDA in H-bond type necessitates additional energy to overcome, further contributing to the disparity in free energy barriers between the two systems. Moreover, an analysis of H-bond type distribution reveals that the slab system is dominated by DDA type, where the ratio of DDAA, DDA, DAA, DA, and Free types are 2%, 75%, 6.6%, 16%, and 0.4%, respectively. Whereas in the nanodroplet (Fig. 2h), the ratio of DDAA, DDA, DAA, DA and Free types are 1.4%, 20%, 0.3%, 76%, and 2.3%, respectively. The prevalence of DA type in the early stage for the nanodroplet, followed by a transition to DDA type during the dissociation, suggests that the reorganization of H-bonds plays a pivotal role in modulating the reaction kinetics, particularly in systems with distinct dimensionality such as two-dimensional slabs and zero-dimensional nanodroplets.

These findings underscore the critical influence of H-bond networks reorganization on the reaction kinetics, highlighting the need for a nuanced understanding of these dynamics to predict and control chemical reactions at the air-water interface. The detailed hydration reaction of furanone and the hydrolysis of SO_2 are illustrated in Supplementary Fig. 8 and Supplementary Fig. 9, respectively.

Electrostatic potential and configuration entropy

The reaction acceleration at microdroplet is primarily driven by the interfacial electric field[42]. Emerging evidence from both experimental and theoretical researches has indicated that the topmost water layer of the air-water interface is predominantly characterized by O-H dangling bonds pointing toward the vapor phase[6,8]. Beneath this layer, a two-dimensional H-bond network oriented parallel to the dynamic surface supports the configuration of free O-H groups. These structural and dynamic features of the air-water interface, which extend approximately two water layers deep, produce electric field signatures distinct from those of the bulk-like interior of the droplet. The theoretical electrostatic potential φ is calculated as the difference between the average plateau values of the bulk liquid and vacuum regions in $\bar{\varphi}(r)$, as described by the equation:

$$\bar{\varphi}(r) = \left\langle \iint \frac{dxdyV(x,y,z)}{A} \right\rangle \quad (1)$$

where $V(x,y,z)$ represents the calculated electrostatic potential at the grid point, and A is the sphere area of nanodroplet at radius of r.

To visualize the spatial distribution of electrostatic potential, Fig. 3a presents the isocontour maps of the electrostatic potential for the slab system and the $(H_2O)_{100}$ nanodroplet, covering a potential range from −13.61 to +13.61 V. The negative potential regions primarily reflect areas of high electron density. In contrast, as the potential increases to positive values, the contours progressively enclose the atomic nuclei, corresponding to the position of protons. To isolate the external electrostatic potential contributions, Kathmann et al.[43] proposed a density-based masking approach for computing the surface potential. This method partitions the spatial grid according to the electron density and includes only regions below a defined threshold, thereby excluding high-density zones near nuclei. The masked potential is defined as:

$$\tilde{\varphi}(r) = \bar{\varphi}(r)\Theta\left[\rho_{elec}^{cutoff} - \rho_{elec}(r)\right] \quad (2)$$

where Θ denotes the Heaviside function ($\Theta(x) = 1$ when $x > 0$; $\Theta(x) = 0$ when $x < 0$). A predefined electron density threshold, ρ_{elec}^{cutoff}, is used to exclude regions with higher electron density from contributing to the surface potential evaluation. This method enables us to examine the relevant phenomena based on the premise that the electron density is lower in the regions between water molecules. We randomly selected 5 snapshot structures from the 10 ns trajectory from machine-learning-assisted simulations to obtain the mean electrostatic potential of slab system and nanodroplet $(H_2O)_{100}$, as shown in Fig. 3b,c. The direction of interfacial electric field is normal to the surface for both nanodroplets and slab system. The surface potential determined with MLP is positive like AIMD[36,43], which is qualitatively different from classical force fields yielding a negative surface potential[6]. Figure 3b presents the variation of the electrostatic potential along the z-direction, calculated by progressively including mesh points associated with lower electron density thresholds (in e/bohr^3). The case labeled with an infinite cutoff represents the scenario where all mesh

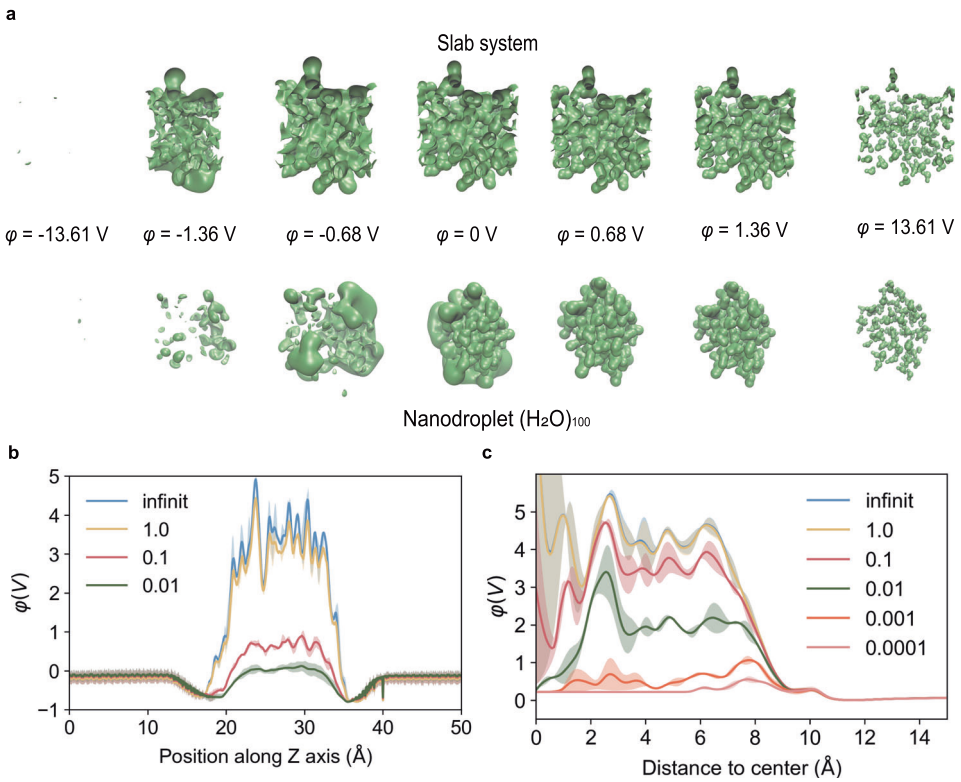

Fig. 3 | Electrostatic potential profiles of the slab system and nanodroplet $(H_2O)_{100}$. **a** Isocontour maps of the electrostatic potential for the slab (upper panel) and $(H_2O)_{100}$ nanodroplet (lower panel) based on quantum mechanical calculations, spanning a potential range of −13.61 to +13.61 V. Regions of negative potentials represent electron-rich domains, while positive potentials are localized around the protonic sites within atomic nuclei. **b** Electrostatic potential profile of the slab system plotted along the z-axis for a series of electron density isocontours (in e/bohr^3). The curve labeled as "infinite" includes the contribution from all mesh points used in the potential calculation. **c** The variations of electrostatic potential by radial regions in the nanodroplet $(H_2O)_{100}$. The shaded areas represent the standard deviation from five snapshot structures.

https://doi.org/10.1038/s41467-025-60298-z

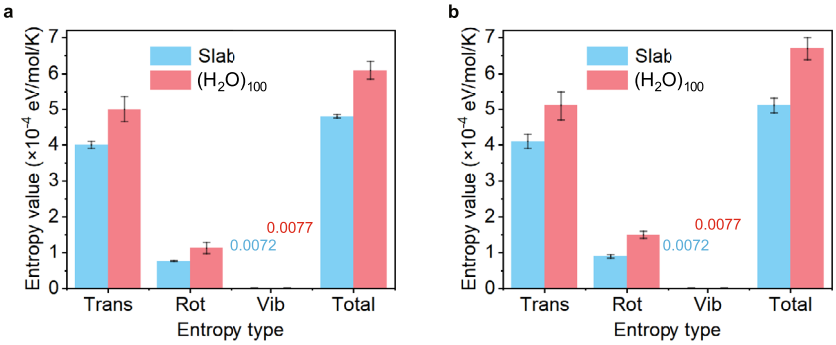

Fig. 4 | Absolute entropy of the slab system and nanodroplet $(H_2O)_{100}$. Absolute entropy of slab system and nanodroplet $(H_2O)_{100}$ composed by the contributions of translation, rotation, and vibration for (**a**) the whole system and (**b**) the corresponding air-water interfacial region. Error bars represent the standard deviation from four trajectories of 20, 50, 100, and 200 ps.

points are considered. It is evident that the distribution of electrostatic potential strongly depends on the choice of electron density contours. As the electron density threshold decreases from 1 to 0.01 e/bohr³, the value of the electrostatic potential declines markedly, from approximately +4 V to nearly 0 V. While for the nanodroplet $(H_2O)_{100}$, the electrostatic potential is the same as slab system at 1 *e*/bohr³, but it is 2 V higher than in the slab system when the electron density is 0.1 and 0.01 *e*/bohr³, eventually decreasing to 0 V until 0.0001 *e*/bohr³, as shown in Fig. 3c. A similar trend is observed for nanodroplets of other sizes, as presented in Supplementary Fig. 10. These results demonstrate that the computed surface potentials for the slab system are very sensitive to the electron density contour level, whereas the nanodroplets are less sensitive to the contour level.

Both computational and experimental results suggest that such interfacial electric field could accelerate the reaction on air-water interface. Song et al.[7] quantitatively calculated a reduction of approximately ~2 kcal/mol in the free barrier for the aza-Michael addition reaction between methylamine and acrylamide, caused by an interfacial electric field of 0.1 V/Å. Zhang's group attributed the fast sulfate production in microdroplets to the ultra-strong electric field at the air-water interface of microdroplet[5]. However, the interfacial electric field of the slab system, as represented in Fig. 3b, is lower than that of nanodroplet, implying that the higher reactivity on slab system may not be strongly correlated with the interfacial electric field.

Beyond the influence of the interfacial electric field, the entropy is calculated to elucidate the difference between nanodroplet and slab system. We calculated absolute entropy by the Schlitter's Formula[44]:

$$S = \frac{\mathrm{R}}{2} \ln \det\left[1 + \frac{\mathrm{k}Te^2}{\hbar} M\sigma\right] \quad (3)$$

where k is Boltzmann's constant, R is the molar gas constant, T is the temperature, e is Euler's number, $\hbar$ is Planck's constant divided by 2π, M is the mass matrix with the masses of the atoms on the diagonal and all off-diagonal elements equal to zero, 1 is the unit matrix, and σ is the covariance matrix of the $3N$ Cartesian coordinates where N is the number of atoms in the considered molecule or molecules. To execute the method, the DoSPT[45] implementation was used. The entropy values of both the whole system (Supplementary Table 4) and air-water interface region (Supplementary Table 5) for the nanodroplet $(H_2O)_{100}$ and slab system are calculated in different temporal scale. As shown in Fig. 4a, the translation (S_{trans}), rotation (S_{rot}), vibration (S_{vib}) and total (S_{total}) entropy of nanodroplet are higher than those of slab system, revealing distinct thermodynamic signatures between nanodroplet and slab systems. Specifically, the total entropy of nanodroplet $(H_2O)_{100}$ is approximately $(6.1 \pm 0.25) \times 10^{-4}$ eV/mol/K, exceeding that of the slab system $(4.8 \pm 0.05) \times 10^{-4}$ eV/mol/K. Strikingly, interfacial entropy values in Fig. 4b show near equivalence between systems $(6.7 \pm 0.3) \times 10^{-4}$ vs. $(5.1 \pm 0.2) \times 10^{-4}$ eV/mol/K, suggesting that the disorder of interfacial water dominates the thermodynamics of nanodroplet.

Size dependent on interfacial water structure

To further reveal the structure difference nanodroplets as a function of size, we present a schematic of the setup used to generate aqueous nanodroplets by spraying a bulk solution with dry inert nebulizing gas, as illustrated in Fig. 5a. Eight nanodroplets system with $(H_2O)_n$ (n = 19, 21, 30, 50, 100, 200, 300, 500), and slab system are used in our simulation. The corresponded radiuses of these nanodroplets are 4.3, 4.6, 5.8, 7.1, 8.9, 11.2, 12.9, and 15.3 Å, respectively. Up to now, the primary challenge lies in characterizing nanodroplets with sizes below the diffraction limit, which exhibit extremely short lifetimes for rapid evaporation, these factors collectively impede investigation in this regime and render the problem difficult to address using conventional characterization techniques[46]. Therefore, it is necessary to conduct a theoretical exploration on the acceleration effect.

To elucidate the vibrational characteristics of water, we conducted the VDOS analysis for a series of water nanodroplets $(H_2O)_n$ (n = 19 ~ 500), as well as bulk water by employing the Fourier transform of velocity autocorrelation functions. The VDOS calculation formula for the water is provided in Supplementary Note 3. As shown in Fig. 5b, the low frequency region around 1000 cm^{-1} is attributed to the librational motions of water molecules, predominantly associated with the rotational mode of water. The simulated librational frequency for bulk water is recorded at 608 cm^{-1}, which closely aligns with the experimentally measured bulk liquid water infrared spectrum at 600 cm^{-1}[47]. For nanodroplets in the size range of $(H_2O)_{19}$ to $(H_2O)_{300}$, the librational frequency peaks exhibit a gradual redshift from 480 to 605 cm^{-1}. When the size of nanodroplet increases to n ≥ 300, the librational frequency peaks keep at 605 cm^{-1}. The high-frequency region of VDOS is indicative of the stretch vibration of O-H bond. The peak for the O-H stretch band of bulk liquid water is observed at 3375 cm^{-1}, approaching to experimental value of bulk liquid water (~3400 cm^{-1})[48]. As the nanodroplet size increases from $(H_2O)_{19}$ to $(H_2O)_{300}$, the O-H stretch band undergo a blueshift from 3470 to 3375 cm^{-1}. For nanodroplets with n ≥ 300, the O-H band peaks also remain consistent at 3375 cm^{-1}. The observed change of O-H stretch band peak as a function of nanodroplet size is consistent with the experimental trends of $H^+(H_2O)_n$[37], suggesting that the nanodroplet as the increase size experiences from gas-liquid-like, disordered structures at smaller sizes (n < 300), to at least partially liquid-like structures at larger sizes (n ≥ 300). The VDOS for different radial region is provided in Supplementary Fig. 11.

Particularly, a shoulder peak in the O-H stretch band for water nanodroplet is identified at around 3700 cm^{-1} due to the presence of free OH groups residing at the air-water interface[49]. Figure 5c shows that the calculated free OH stretch frequency based on the machine learning potentials (MLPs) are linearly proportional to the $n^{-2/3}$ or $1/r^2$, where n is the number of water molecules in the nanodroplet, and r represents the nanodroplet effective radius. The free OH stretch frequency as the change of number of water molecules in nanodroplet increases linearly from 3697 to 3710 cm^{-1}. Extrapolations of the infrared photodissociation (IRPD) data[50] to infinite cluster size yields a free OH stretch frequency centered on ~3698 cm^{-1} and the MLP data is centered on ~3697 cm^{-1}. This trend using MLPs is also well consistent with the experiment measured by IRPD, while the OPLS-2005 model[50] demonstrates a close agreement with the experimental frequencies, with an average deviation of approximately 14 cm^{-1}, and the ReaxFF/CGeM model[6] even deviates by an average of approximately 180 cm^{-1}.

The asymmetric stretching frequencies generated by the free O-H of the water molecules at the surface are acutely sensitive to H-bond networks. To delve deeper into this relationship, we further analyze the variations coordination unsaturation (CU) across the region of air-water interface of nanodroplets as a function of the radius of water nanodroplets, where the CU is defined by the below equation:

$$\mathrm{CU} = \frac{\text{The reduced number of hydrogen bonds at interface}}{\text{The total number of hydrogen bonds}} \quad (4)$$

where the "reduced number of hydrogen bonds" is the difference between the maximum possible number of H-bonds that a molecule could form in a fully coordinated environment (4 H-bonds) and the actual number of H-bonds formed by the surface molecules. As depicted in Fig. 5d, the CU of nanodroplets exhibits a pronounced size dependence within the nanometer scale, suggesting an approximate inverse proportionality to the droplet size. When the nanodroplet size reaches to 1.5 nm, the CU approaches about 13%, which is already very close to the absence of one coordination per water molecule. This phenomenon can be attributed to the elevated surface-to-volume ratio in nanodroplets, leading to a higher proportion of surface molecules that do not participate in H-bond network.

As the radius of nanodroplet increases, the relative influence of surface molecules diminishes, resulting in a H-bond network that more closely resembles that of the bulk. It is worth note that the CU is proportional to the Gibbs-Thompson equation:

$$\mathrm{CU} \propto \exp\left(\frac{2\gamma V_m}{rRT}\right) \quad (5)$$

Here, r is the effective radius of the nanodroplet, γ is the specific surface tension, V_m is the molar volume of the material, R is the gas constant, and T is the absolute temperature. In the Gibbs−Thompson Eq. (5), the theoretical treatments presented in this section are based on the assumption that all surface atoms experience the same amount of surface tension, regardless of their position or the size and shape of the nanodroplet[51]. This assumption is equivalent to assuming the surface tension value of slab system (72 mN/m)[40]. This equation highlights the relationship between the surface energy and size of the nanodroplet with a nonlinear effect. The Gibbs-Thomson effect articulates the interplay between the size of the nanodroplet and its phase transition temperatures, with smaller nanodroplets demonstrating reduced melting points relative to bulk materials due to their increased surface-to-volume ratio. In the field of chemical reactions, nanodroplets act as highly reactive sites due to their large surface area and unique surface properties. The Gibbs-Thomson effect helps understanding the reactivity patterns of these nanodroplets, thereby enabling the design of efficient catalysts for various chemical processes. Moreover, by extrapolation from the Gibbs-Thompson equation, the CU becomes negligible, less than 10%, when the nanodroplet size exceeds approximately 10 nm.

The change of CU reflects distinct reorientation dynamics of water molecules. These orientational dynamics, intricately linked to relaxation timescales, are largely dependent on the local environment. The H-bond rearrangements, known as jumps, also contribute to this process. We quantified the average timescale associated with the critical dynamics of restructuring the H-bond network of water via the dipole autocorrelation function, as represented in Fig. 6a. The dipole of water is approximately defined using the classical SPC/E model[52], where the dipole moment is calculated based on the positions and charges of the individual atoms in the water molecule, as shown in Supplementary Fig. 17. The dipole autocorrelation function is provided in Supplementary Note 2. The rotational dynamics are slowest in the bulk system, which is consistent with Chen et al.'s calculation[53]. The mechanism for rotational relaxation of the O-H bond vector is associated with breaking an H-bond. In order to build our intuition on the vary of rotation, Fig. 6b highlights a specific event of slab system and representative nanodroplet $(H_2O)_{100}$, illustrating a close-up of several of these molecules distributed on bulk and air-water interface of slab system and nanodroplet. Shown in the background are all the other water molecules in close vicinity to this event. The black arcs are the smallest and outline the rotation of water molecules in bulk liquid water, where H-bonds are too strong, significantly hindering this pathway. The rotational motion of water of slab system at the air-water interface decays faster than that of the bulk system due to the relax H-bonds network at the air-water interface, corresponding to that the blue arcs is bigger than black arcs. The rotational motion of water at the air-water interface of nanodroplets shows a faster decay with decreasing nanodroplet size. The rotation motion of the whole nanodroplet exhibits a similar trend (Supplementary Fig. 12). As the size of nanodroplets decreases, the surface-to-volume ratio increases, resulting in a greater proportion of water molecules being influenced by surface effects. This enhances the rotation dynamics, as surface water molecules experience fewer H-bonds and are more mobile compared to those in the bulk. The high curvature causes a distortion in the H-bond network, which can further accelerate the rotation dynamics. The red arcs represent the fast rotation of water molecule at the air-water interface of nanodroplets $(H_2O)_{100}$. Figure 6c shows the mean square displacement (MSD) for water molecules in various sized water droplets. The diffusion of water molecules in the smaller nanodroplet is higher than that in the larger nanodroplet. Thus, water molecules in the smaller nanodroplet have more rotate energy and transfer energy. The increase in both rotational and translational energy indicates that the energy is dissipated between these modes, rather than being transferred into the reaction itself.

To further analysis the H-bond networks, we calculate the H-bond type distribution at air-water interface of $(H_2O)_n$ (n = 19, 21, 30, 50, 100, 200, 300, 500) and slab system, as plotted in Fig. 6d, the ratio refers to the fraction/percentage population. A common definition of a water H-bond is one where $D_{OO} < 3.5$ Å and $\theta < 30°$. Each bulk water molecule possesses an average of ~3.47 H-bond in a homogeneous solvent environment, which is close to the theoretical calculation value of 3.58 reported by Lin et al.[54]. At the air-water interface, DA is the dominant component of the H-bond networks for nanodroplets, while in the slab system, the DDAA, DDA, DAA, and DA configurations are evenly distributed. The uniformity of the nanodroplet structure indicates a more ordered H-bond network configuration in the droplet. With n increasing from 19 to 500, the ratio of DA decreases from 0.65 to 0.34, and the ratio of DDAA increases from 0.008 to 0.13. However, the DAA, DDA, and Free H-bonds do not have a stable vary trend, fluctuating within 0.1 ~ 0.25 due to unstable H-bond structure with the fast rotate water molecules. The H-bond type distribution of the whole system

https://doi.org/10.1038/s41467-025-60298-z

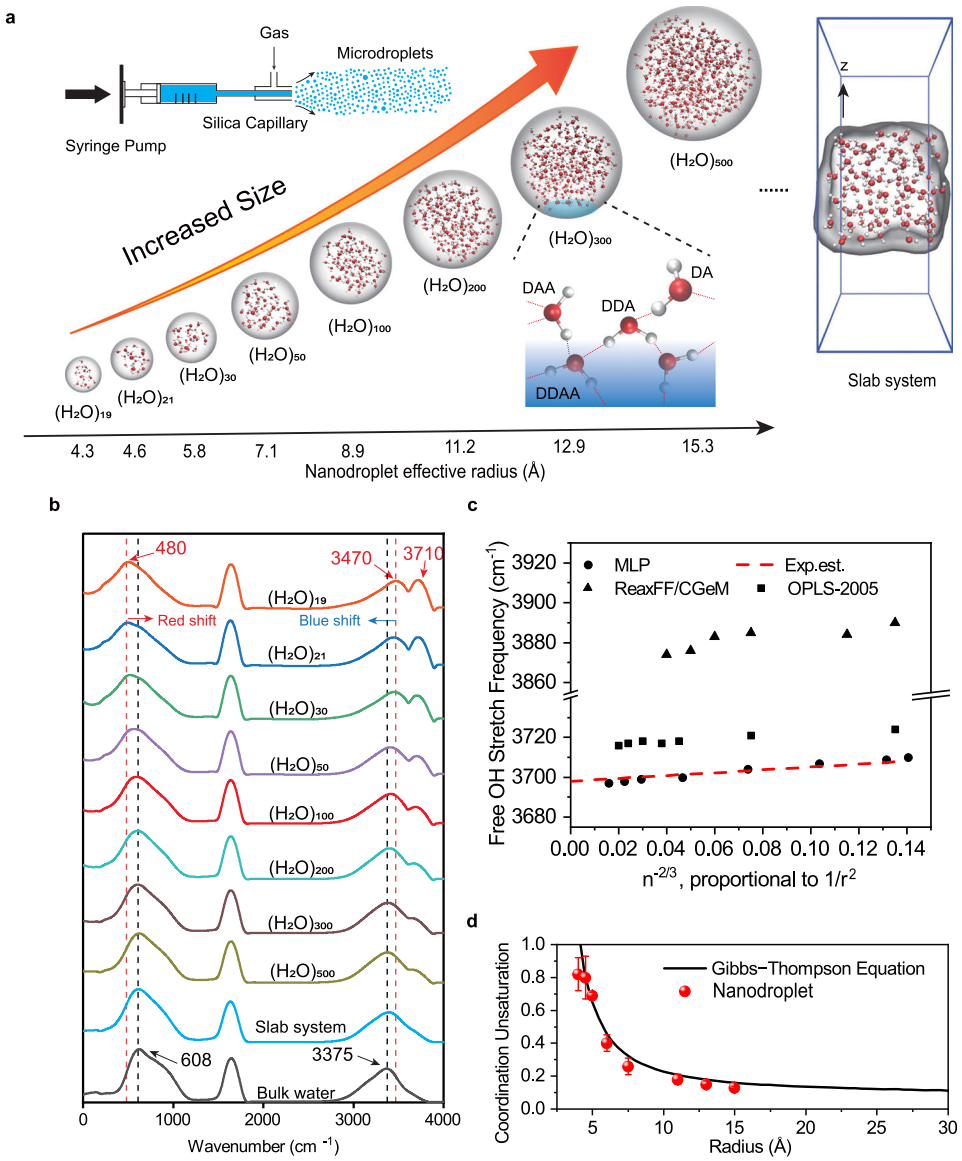

Fig. 5 | Schematic illustrations of the nanodroplets of different size with the structural feature. a Schematic diagram of a conventional device for generating droplets and water nanodroplet model for simulation in different size $(H_2O)_n$ ($n = 19$, 21, 30, 50, 100, 200, 300, 500), as well as slab system with 512 water molecules. Aqueous nanodroplets were generated by spraying bulk solution using dry inert nebulizing gas without applying an external voltage to the spray source. On the air-water interface of nanodroplets, H-bonded water molecules with different donor (D) and acceptor (A) H-bonds are represented. This picture was created using Adobe Illustrator. **b** The VDOS of hydrogen atoms in the nanodroplets of various sizes, including $(H_2O)_{19}$, $(H_2O)_{21}$, $(H_2O)_{30}$, $(H_2O)_{50}$, $(H_2O)_{100}$, $(H_2O)_{200}$, $(H_2O)_{300}$, $(H_2O)_{500}$, slab system, and bulk liquid water. **c** Here we compared free OH bands from experiments and theory for $(H_2O)_n$ as a function of $n^{-2/3}$, which is proportional to $1/r^2$ where r is the droplet radius. The red dash line represents the experimental results, the circle dots represent the result from MLP and the triangles are the result using the ReaxFF/CGeM force field[6], as well as the square represents the result using the OPLS-2005 force field[50]. **d** The variations in surface CU by the radius of water nanodroplets. The red points with arrow bar and black line represent the surface CU for $(H_2O)_n$ ($n = 19$, 21, 30, 50, 100, 200, 300, 500), and the Gibbs-Thompson equation of water, respectively. Error bars represent the standard deviation from 100000 snapshot structures.

could be found in Supplementary Fig. 13. Water molecules exhibit a dangling O-H bond with a reduced average number of H-bond. From a static structural perspective, the O•••O distance and the O-H bond length between two water molecules involved in H-bond generally adhere to the principles of asymmetrical H-bond cooperativity and polarizability. From the nanodroplet interface to interior, the O•••O distance decreases while the O-H distance increases due to the enhanced H-bonds (Supplementary Fig. 14 and Supplementary Table 2). These variations highlight the significant influence of size and surface effects on the H-bond network and reorientation dynamics of water molecules.

Numerous experimental and theoretical studies have demonstrated that reaction rates are highly sensitive to variations in the H-bond networks. This study found that changes in nanodroplet size significantly alter the coordination unsaturation at the interface, triggering pronounced structural shifts within the H-bond network type. However, the associated rotational and translational energy changes do not appear to influence the reaction directly. Instead, it is the variation in the configuration entropy of the H-bond network that plays a pivotal role in regulating the reaction rate. When the nanodroplet radius increases to around 15 Å, the distribution of H-bond types becomes remarkably similar to that observed in slab systems, suggesting that their interfacial catalytic effects are likewise comparable. This discovery provides new insights into catalytic reactions at air-water interfaces and opens avenues for optimizing the design of nanoreactors to enhance catalytic efficiency.

https://doi.org/10.1038/s41467-025-60298-z

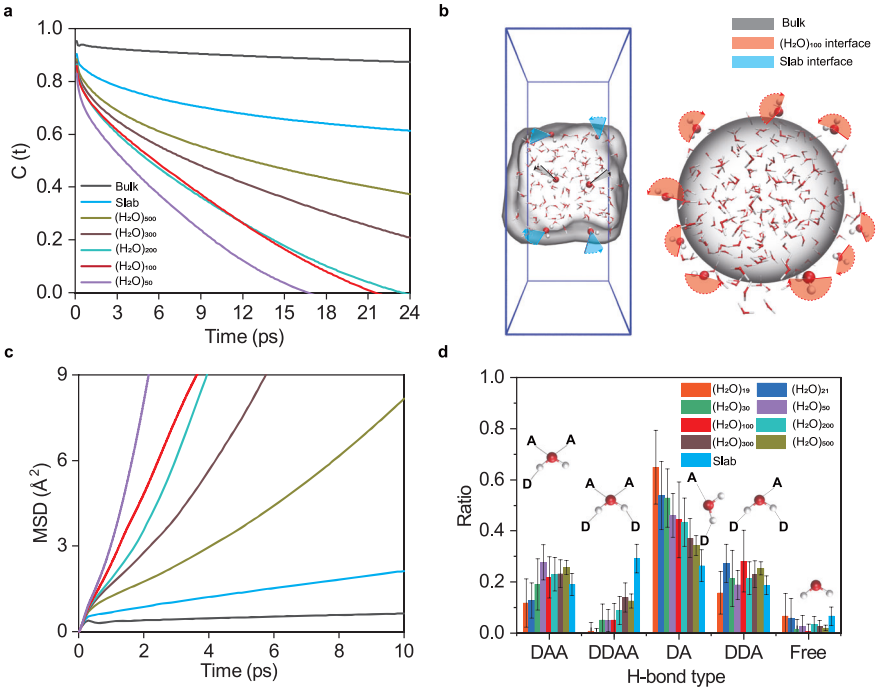

Fig. 6 | Asymmetrical dynamic and H-bond structural analysis of various water nanodroplets. a Dipolar rotational autocorrelation curves of water molecules at the air-water interface of the $(H_2O)_n$ (n = 50, 100, 200, 300, 500) and the slab system, compared with bulk water. **b** Schematic of rotation of water molecules. Close-ups of 15 of these molecules are presented in slab system and $(H_2O)_{100}$. The colored arcs outline the angular motion carried by the dipole vectors in the direction of the dashed arrow. The black stands for the water molecules in the bulk, as well as the blue and red represent the water molecules at the air-water interface of slab system and $(H_2O)_{100}$. This picture was created using Visual Molecular Dynamics. **c** The MSD profiles for nanodroplet $(H_2O)_n$ (n = 19, 21, 30, 50, 100, 200, 300, 500), slab system, and bulk liquid water. **d** The ratio of H-bond type of nanodroplet $(H_2O)_n$ (n = 19, 21, 30, 50, 100, 200, 300, 500) and slab system at air-water interface. Error bars represent the standard deviation from 10000 snapshot structures.

Discussion

In this study, we quantitatively demonstrated the critical influence of the H-bond network on the reactivity of interfacial water at the air-water interface, particularly in contrasting slab and nanodroplets. Our ab initio molecular metadynamics simulations revealed that the H-bond network type in nanodroplets gets stuck in the formation of donor-acceptor dimers, which significantly hinders the adaptability of interfacial water for chemical reactions. In contrast, the more homogeneous H-bond motif in slab facilitates a 1–2 kcal/mol lower free energy barrier, resulting in an order of magnitude faster reaction rate. This difference in reactivity arises from the measured variation in solvation configurational entropy between the nanodroplet and the slab surface under ambient conditions. Furthermore, the VDOS demonstrates a linear correlation between the free O-H stretching frequency and the inverse square of the nanodroplet size, with the variation in interfacial coordination unsaturation aligning with predictions from the Gibbs-Thomson equation. As the nanodroplet size decreases, the restructuring of the H-bond network leads to faster rotational dynamics and translation of interfacial water molecules. However, while the increased energy is not directly transferred to the reaction, it may be dissipated between rotational and translational modes. These findings underscore the crucial role of H-bond network structure in tuning catalytic performance at the air-water interfaces, offering a potential pathway for optimizing catalytic systems in both scientific and industrial applications.

Methods

Database

The primary database collection was achieved through AIMD simulations. Density functional theory (DFT) was employed within the CP2K/Quickstep framework[55], utilizing a hybrid Gaussian plane wave (GPW) scheme. Wave function optimization was performed using matrix diagonalization, and self-consistent field (SCF) convergence was achieved at an electronic temperature of 298.15 K with the aid of Fermi smearing. The core electrons were represented by Goedecker-Teter-Hutter (GTH)[56] pseudopotentials and DZVP-MOLOPT-SR-GTH basis sets, and the energy cutoff for the plane wave expansion was set to 400 Ry. The exchange-correlation effects were described using the Perdew-Burke-Ernzerhof (PBE) functionals[57], and dispersion corrections were applied using the Grimme D3 method[58] in all calculations. $(H_2O)_{19}$, $(H_2O)_{21}$, $(H_2O)_{30}$, $(H_2O)_{50}$, and $(H_2O)_{100}$, as well as bulk and slab systems were run for 30 ps, and $(H_2O)_{200}$ system was run for 10 ps. $(H_2O)_{300}$ and $(H_2O)_{500}$ were run for 3 ps due to their huge amount of computation. The dimensions of the simulation boxes are provided in Supplementary Table 1. A Langevin thermostat was employed to maintain a temperature of 298.15 K with a time step of 0.5 fs. The training set could be found in Supplementary Fig. 1.

Training of machine learning potential

We selected a dataset comprising 3000 structures from $(H_2O)_{19}$, $(H_2O)_{21}$, $(H_2O)_{30}$, $(H_2O)_{50}$, $(H_2O)_{100}$, bulk, and slab systems trajectories of the aforementioned AIMD simulations. Additionally, we included 1000 structures from $(H_2O)_{200}$ trajectories and 300 structures from $(H_2O)_{300}$ and $(H_2O)_{500}$ trajectories to serve as the initial dataset. Machine learning potential was fitted with deep potential smooth edition (DeePMD-SE) kit[59,60]. In accordance with the provided dataset, four MLPs were trained using deep neural networks during the training process, each with different initial parameters. Subsequently, during the exploration phase, one of the four MLPs was employed to drive machine learning molecular dynamics, and maximum force deviations ($\sigma_f^{\max} = \max\sqrt{\left\langle \|f_i - \langle f_i \rangle\|^2 \right\rangle}$) among four MLPs were calculated

along the trajectories. For each nanodroplet, 100 structures with $\sigma_f^{\max} \in (\sigma^{low}, \sigma^{high}]$ were randomly selected and computed using DFT, then added to the datasets for the subsequent iteration. σ^{low} and σ^{high} were set to 0.1 and 0.25, respectively. The iterative training would finish when $\sigma_f^{\max}$ of all structures in trajectories are less than σ^{low}. To validate the accuracy of MLP, we demonstrate an excellent agreement between the RDF of water obtained from the MLP model (solid line in Supplementary Fig. 2) and the results from AIMD simulations (dotted line in Supplementary Fig. 2). This concurrence demonstrates that the trained potential energy surface effectively captures the structural characteristics. The AIMD simulations of the nanodroplets, bulk, and slab systems are directly correlated with the force and energy profiles of the MLPs, as illustrated in Supplementary Fig. 3 and Supplementary Fig. 4. To quantify the agreement between the predicted and reference values, the root mean square error (RMSE) calculations for force and energy are calculated by equation:

$$F_{RMSE} = \sqrt{\frac{\sum_{i=1}^{3M}\left(F_i^{AIMD} - F_i^{MLP}\right)^2}{3M}} \quad (6)$$

where F_{RMSE} represents the RMSE of the force, $i = 1$ to $3M$ represents the component forces in the three directions of x, y, and z. F_{AIMD} represents the force obtained by AIMD, and F_{MLP} represents the force obtained by the trained potential energy surface. The RMSE of energy is calculated in the same way as the RMSE of force.

MD simulations

Finally, we used the trained potential energy surface to perform MD simulations using the large-scale atomic/molecular massively parallel simulator (LAMMPS) code[61]. We employed the canonical ensemble (NVT) with a target temperature of 300 K and a time step of 0.5 fs. The simulations were run for 10 ns to obtain the desired sampling. Other settings remained similar to the initial AIMD setup. Density distribution (Supplementary Fig. 5), triplet angular distribution (Supplementary Fig. 6), electrostatic potential, VDOS and H-bond analysis on machine learning MD trajectories are then applied to reveal the nanodroplet size-property relation. The general workflow is presented in Supplementary Fig. 1.

Metadynamics-biased AIMD simulation details

We chose $(H_2O)_{100}$ as a representative nanodroplet to compare three reactions with the slab system containing 128 water molecules. A single sulfur dioxide (SO_2) molecule and a five-membered ring were added to both the nanodroplet and slab surface systems to investigate their reaction with water molecules. Both energy minimization and pre-equilibrium were performed using the cp2k software package[55]. For pre-equilibrium, the Becke-Lee-Yang-Parr (BLYP) functionals[57], with Grimme's[58] dispersion corrections and Becke-Johnson[62] damping term, and the double-ζ plus polarization (DZVP) basis set were used. An energy cutoff of 300 Ry was set for the plane-wave basis set and 40 Ry cutoff was used for the Gaussian basis set. The core electrons were modeled using Goedecker-Teter-Hutter[63] (GTH) norm-conserving pseudopotentials. The AIMD simulations were performed in the canonical (NVT) ensemble, with a temperature of 298.15 K controlled using canonical sampling through velocity rescaling thermostat[64] (CSVR). The time step for was set for 1.0 fs. Three independent metadynamics simulations with randomly selected initial structures were performed to determine the reaction free profiles. The water self-dissociation, the hydrolysis of SO_2 and the hydration reaction of furanone take 45 ps, 350 ps, and 250 ps, respectively. The error bars were calculated based on the standard deviation from three independent simulations. Further details regarding the metadynamics-biased AIMD simulation are provided in the Supplementary Methods.

Data availability

The metadynamics input file, the deep potential models generated in this study, the initial and final coordinates of electronic structure calculations trajectories and source data are available at https://zenodo.org/records/15208621.

Code availability

The metadynamics simulations were performed by CP2K. Deep potential molecular dynamics simulations were conducted using the DeePMD-kit package (https://github.com/deepmodeling/deepmd-kit) in conjunction with LAMMPS. The code used to generate the plots shown in the main text is available from the corresponding author upon request.

References

1. Ruiz-Lopez, M. F., Francisco, J. S., Martins-Costa, M. T. C. & Anglada, J. M. Molecular reactions at aqueous interfaces. *Nat. Rev. Chem.* **4**, 459–475 (2020).
2. Nguyen, D., Lyu, P. & Nguyen, S. C. Experimental and thermodynamic viewpoints on claims of a spontaneous H2O2 formation at the air–water Interface. *J. Phys. Chem. B.* **127**, 2323–2330 (2023).
3. Sun, Q. et al. Understanding hydrogen electrocatalysis by probing the hydrogen-bond network of water at the electrified Pt–solution interface. *Nat. Energy.* **8**, 859–869 (2023).
4. Li, M. et al. Comprehensive understandings of hydrogen bond chemistry in aqueous batteries. *Adv. Mater.* **36**, 2308628 (2024).
5. Liu, Y. et al. Strong electric field force at the air/water interface drives fast sulfate production in the atmosphere. *Chem* **10**, 330–351 (2024).
6. Hao, H., Leven, I. & Head-Gordon, T. Can electric fields drive chemistry for an aqueous microdroplet? *Nat. Commun.* **13**, 280 (2022).
7. Song, Z. et al. Deciphering the microdroplet acceleration factors of Aza-Michael addition reactions. *J. Am. Chem. Soc.* **146**, 10963–10972 (2024).
8. Xiong, H., Lee, J. K., Zare, R. N. & Min, W. Strong electric field observed at the interface of aqueous microdroplets. *J. Phys. Chem. Lett.* **11**, 7423–7428 (2020).
9. Li, P. et al. Hydrogen bond network connectivity in the electric double layer dominates the kinetic pH effect in hydrogen electrocatalysis on Pt. *Nat. Catal.* **5**, 900–911 (2022).
10. Verduci, R. et al. Water structure in the first layers on TiO2: a key factor for boosting solar-driven water-splitting performances. *J. Am. Chem. Soc.* **146**, 18061–18073 (2024).
11. Freda, M., Piluso, A., Santucci, A. & Sassi, P. Transmittance fourier transform infrared spectra of liquid water in the whole mid-infrared region: temperature dependence and structural analysis. *Appl. Spectrosc.* **59**, 1155–1159 (2005).
12. Smedley, S. B., Chang, Y., Bae, C. & Hickner, M. A. Measuring water hydrogen bonding distributions in proton exchange membranes using linear Fourier Transform Infrared spectroscopy. *Solid State Ionics* **275**, 66–70 (2015).
13. Stirnemann, G., Rossky, P. J., Hynes, J. T. & Laage, D. Water reorientation, hydrogen-bond dynamics and 2D-IR spectroscopy next to an extended hydrophobic surface. *Faraday. Discuss.* **146**, 263–281 (2010).
14. Mitsui, T., Rose, M. K., Fomin, E., Ogletree, D. F. & Salmeron, M. Water Diffusion and Clustering on Pd(111). *Science* **297**, 1850–1852 (2002).
15. Morgenstern, K. & Rieder, K.-H. Formation of the cyclic ice hexamer via excitation of vibrational molecular modes by the scanning tunneling microscope. *J. Chem. Phys.* **116**, 5746–5752 (2002).
16. Michaelides, A. & Morgenstern, K. Ice nanoclusters at hydrophobic metal surfaces. *Nat. Mater.* **6**, 597–601 (2007).

17. Wang, Y.-H. et al. In situ Raman spectroscopy reveals the structure and dissociation of interfacial water. *Nature* **600**, 81–85 (2021).
18. Wang, Y.-H. et al. Characterizing surface-confined interfacial water at graphene surface by in situ Raman spectroscopy. *Joule* **7**, 1652–1662 (2023).
19. You, X. et al. Exploring the cation regulation mechanism for interfacial water involved in the hydrogen evolution reaction by in situ raman spectroscopy. *Nano-Micro Lett.* **16**, 53 (2023).
20. Li, C.-Y. et al. In situ probing electrified interfacial water structures at atomically flat surfaces. *Nat. Mater.* **18**, 697–701 (2019).
21. Fenter, P. & Sturchio, N. C. Mineral–water interfacial structures revealed by synchrotron X-ray scattering. *Prog. Surf. Sci.* **77**, 171–258 (2004).
22. Ye, Y. et al. Using soft x-ray absorption spectroscopy to characterize electrode/electrolyte interfaces in-situ and operando. *J. Electron. Spectrosc.* **221**, 2–9 (2017).
23. Velasco-Velez, J.-J. et al. The structure of interfacial water on gold electrodes studied by x-ray absorption spectroscopy. *Science* **346**, 831–834 (2014).
24. Wu, L., Wang, X., Wang, G. & Chen, G. In situ x-ray scattering observation of two-dimensional interfacial colloidal crystallization. *Nat. Commun.* **9**, 1335 (2018).
25. Wang, Y. et al. Chemistry governs water organization at a graphene electrode. *Nature* **615**, E1–E2 (2023).
26. Xu, Y., Ma, Y.-B., Gu, F., Yang, S.-S. & Tian, C.-S. Structure evolution at the gate-tunable suspended graphene–water interface. *Nature* **621**, 506–510 (2023).
27. Backus, E. H. G., Schaefer, J. & Bonn, M. Probing the mineral–water interface with nonlinear optical spectroscopy. *Angew. Chem. Int. Edit.* **60**, 10482–10501 (2021).
28. Wang, Y. et al. Direct probe of electrochemical pseudocapacitive pH jump at a graphene electrode. *Angew. Chem. Int. Edit.* **62**, e202216604 (2023).
29. Wang, Y. et al. Heterodyne-detected Sum-Frequency Generation vibrational spectroscopy reveals aqueous molecular structure at the suspended graphene/water interface. *Angew. Chem. Int. Edit.* **63**, e202319503 (2024).
30. Björneholm, O. et al. Water at Interfaces. *Chem. Rev.* **116**, 7698–7726 (2016).
31. Forster, R. J., Keyes, T. E. & Majda, M. Homogeneous and heterogeneous electron transfer dynamics of osmium-containing monolayers at the air/water interface. *J. Phys. Chem. B.* **104**, 4425–4432 (2000).
32. Hsieh, C.-S. et al. Aqueous heterogeneity at the air/water interface revealed by 2D-HD-SFG spectroscopy. *Angew. Chem. Int. Edit.* **53**, 8146–8149 (2014).
33. Wei, Z., Li, Y., Cooks, R. G. & Yan, X. Accelerated reaction kinetics in microdroplets: overview and recent developments. *Annu. Rev. Phys. Chem.* **71**, 31–51 (2020).
34. Iyer, K. et al. Accelerated multi-reagent copper catalysed coupling reactions in micro droplets and thin films. *React. Chem. Eng.* **3**, 206–209 (2018).
35. Li, Y., Yan, X. & Cooks, R. G. The role of the interface in thin film and droplet accelerated reactions studied by competitive substituent effects. *Angew. Chem. Int. Edit.* **55**, 3433–3437 (2016).
36. Leung, K. Surface potential at the air–water interface computed using density functional theory. *J. Phys. Chem. Lett.* **1**, 496–499 (2010).
37. Mizuse, K., Mikami, N. & Fujii, A. Infrared spectra and hydrogen-bonded network structures of large protonated water clusters H+(H2O) (n=20–200). *Angew. Chem. Int. Edit.* **49**, 10119–10122 (2010).
38. Behler, J. Perspective: machine learning potentials for atomistic simulations. *J. Chem. Phys.* **145**, 170901 (2016).
39. Sun, C. Q., Huang, Y., Zhang, X., Ma, Z. & Wang, B. The physics behind water irregularity. *Phys. Rep.* **998**, 1–68 (2023).
40. Hauner, I. M., Deblais, A., Beattie, J. K., Kellay, H. & Bonn, D. The dynamic surface tension of water. *J. Phys. Chem. Lett.* **8**, 1599–1603 (2017).
41. Zhao, Z. et al. Understanding hygroscopic nucleation of sulfate aerosols: combination of molecular dynamics simulation with classical nucleation theory. *J. Phys. Chem. Lett.* **10**, 1126–1132 (2019).
42. Martins-Costa, M. T. C. & Ruiz-López, M. F. Electrostatics and chemical reactivity at the air–water interface. *J. Am. Chem. Soc.* **145**, 1400–1406 (2023).
43. Kathmann, S. M., Kuo, I. F. W., Mundy, C. J. & Schenter, G. K. Understanding the surfacepotential of water. *J. Phys. Chem. B.* **115**, 4369–4377 (2011).
44. Carlsson, J. & Åqvist, J. Absolute and relative entropies from computer simulation with applications to ligand binding. *J. Phys. Chem. B.* **109**, 6448–6456 (2005).
45. Caro, M. A., Laurila, T. & Lopez-Acevedo, O. Accurate schemes for calculation of thermodynamic properties of liquid mixtures from molecular dynamics simulations. *J. Chem. Phys.* **145**, 244504 (2016).
46. Yan, X., Bain, R. M. & Cooks, R. G. Organic reactions in microdroplets: reaction acceleration revealed by mass spectrometry. *Angew. Chem. Int. Edit.* **55**, 12960–12972 (2016).
47. Bertie, J. E. & Lan, Z. Infrared intensities of liquids XX: the intensity of the OH stretching band of liquid water revisited, and the best current values of the optical constants of H2O(l) at 25 °C between 15,000 and 1 cm-1. *Appl. Spectrosc.* **50**, 1047–1057 (1996).
48. Maréchal, Y. The molecular structure of liquid water delivered by absorption spectroscopy in the whole IR region completed with thermodynamics data. *J. Mol. Struct.* **1004**, 146–155 (2011).
49. Hsieh, C. S. et al. Mechanism of vibrational energy dissipation of free OH groups at the air-water interface. *Proc. Natl. Acad. Sci.* **110**, 18780–18785 (2013).
50. Cooper, R. J., O'Brien, J. T., Chang, T. M. & Williams, E. R. Structural and electrostatic effects at the surfaces of size- and charge-selected aqueous nanodrops. *Chem. Sci.* **8**, 5201–5213 (2017).
51. Peng, Z. A. & Peng, X. Nearly Monodisperse and Shape-Controlled CdSe Nanocrystals via Alternative Routes: Nucleation and Growth. *J. Am. Chem. Soc.* **124**, 3343–3353 (2002).
52. Berendsen, H. J. C., Grigera, J. R. & Straatsma, T. P. The missing term in effective pair potentials. *J. Phys. Chem.* **91**, 6269–6271 (1987).
53. Chen, M. et al. Ab initio theory and modeling of water. *Proc. Natl. Acad. Sci.* **114**, 10846–10851 (2017).
54. Lin, I. C., Seitsonen, A. P., Tavernelli, I. & Rothlisberger, U. Structure and dynamics of liquid water from ab initio molecular dynamics-comparison of BLYP, PBE, and revPBE density functionals with and without van der waals corrections. *J. Chem. Theory. Comput.* **8**, 3902–3910 (2012).
55. Kühne, T. D. et al. CP2K: An electronic structure and molecular dynamics software package - Quickstep: Efficient and accurate electronic structure calculations. *J. Chem. Phys.* **152**, 194103 (2020).
56. Goedecker, S., Teter, M. & Hutter, J. Separable dual-space Gaussian pseudopotentials. *Phys. Rev. B. Condens. Matter.* **54**, 1703–1710 (1996).
57. Perdew, J. P., Burke, K. & Ernzerhof, M. Generalized gradient approximation made simple. *Phys. Rev. Lett.* **77**, 3865–3868 (1996).
58. Grimme, S., Antony, J., Ehrlich, S. & Krieg, H. A consistent and accurate ab initio parametrization of density functional dispersion correction (DFT-D) for the 94 elements H-Pu. *J. Chem. Phys.* **132**, 154104 (2010).
59. Zhang, L., Han, J., Wang, H. & Car R, E. W. Deep potential molecular dynamics: a scalable model with the accuracy of quantum mechanics. *Phys. Rev. Lett.* **120**, 143001 (2018).

60. Zhang, L. et al. End-to-end symmetry preserving inter-atomic potential energy model for finite and extended systems. *Adv. Neural Inf. Process.* **31**, 4436–4446 (2018).
61. Thompson, A. P. et al. LAMMPS - a flexible simulation tool for particle-based materials modeling at the atomic, meso, and continuum scales. *Comput. Phys. Commun.* **271**, 108171 (2022).
62. Johnson, E. R. & Becke, A. D. A post-Hartree-Fock model of intermolecular interactions: inclusion of higher-order corrections. *J. Chem. Phys.* **124**, 174104 (2006).
63. Goedecker, S., Teter, M. & Hutter, J. Separable dual-space Gaussian pseudopotentials. *Phys. Rev. B.* **54**, 1703–1710 (1996).
64. Bussi, G., Donadio, D. & Parrinello, M. Canonical sampling through velocity rescaling. *J. Chem. Phys.* **126**, 014101 (2007).

Acknowledgements

We thank Dr. Xiaojun Zhou, Prof. Chongqin Zhu, Prof. Yurui Gao, and Prof. Lianrui Hu for useful discussions. J.Y. thanks the support of National Natural Science Foun-dation of China (Grant No. 22203032). P.G. thanks the support of the National Natural Science Foundation of China (Grant No. 12104287). X.H. was supported by the National Natural Science Foundation of China (Grant Nos. 92477103 and 22273023), Shanghai Municipal Natural Science Foundation (Grant No. 23ZR1418200), the Natural Science Foundation of Chongqing, China (Grant No. CSTB2023NSCQ-MSX0616), the Shanghai Frontiers Science Center of Molecule Intelligent Syntheses, Shanghai Future Discipline Program (Quantum Science and Technology), Guizhou Provincial Science and Technology Projects, China (CXTD 2022001), Shanghai Municipal Education Commission's "Artificial Intelligence-Driven Research Paradigm Reform and Discipline Advancement Program" and the Fundamental Research Funds for the Central Universities. We also acknowledge the Supercomputer Center of East China Normal University (ECNU Multi-functional Platform for Innovation 001) for providing computer resources.

Author contributions

J. Y. and X. H. provided continuous supervision throughout the project. J. Y., P.G., and S.C. conceived the ideas and designed the research. S.C. carried out all the simulation, and S.C., J.Z., J.L., and P.G. contributed to data analysis and manuscript preparation.

Competing interests

The authors declare no competing interests.

Additional information

Supplementary information The online version contains supplementary material available at https://doi.org/10.1038/s41467-025-60298-z.

Correspondence and requests for materials should be addressed to Pan Guo, Jinrong Yang or Xiao He.

Peer review information *Nature Communications* thanks the anonymous reviewer(s) for their contribution to the peer review of this work. A peer review file is available.